Supporting Information (SI) for "Preservation of Topological Surface States in Millimeter-Scale Transferred Membranes"

Chi Ian Jess Ip,[†,‡,§] Qiang Gao,[†,§] Khanh Duy Nguyen,[†] Chenhui Yan,[†] Gangbin Yan,[†] Eli Hoenig,[†] Thomas S. Marchese,[†] Minghao Zhang,[¶] Woojoo Lee,[†] Hossein Rokni,[†] Ying Shirley Meng,[†,¶] Chong Liu,[†] and Shuolong Yang[*,†]

†*Pritzker School of Molecular Engineering, University of Chicago, Chicago, IL 60637, USA*

‡*Current address: Department of Physics, Massachusetts Institute of Technology, Cambridge, MA 02139, USA*

¶*Department of NanoEngineering, University of California San Diego, La Jolla, CA 92093, USA*

§*These authors contributed equally to this work.*

E-mail: yangsl@uchicago.edu

SI Note 1: Layer-by-layer growth of Bi_2Se_3 films

High-quality Bi_2Se_3 thin films are grown on 0.05wt% Nb-doped $SrTiO_3$ (111) substrates by molecular beam epitaxy (MBE). The $SrTiO_3$ (111) substrates are annealed at 1000°C for 30 minutes in the MBE chamber to obtain an atomically flat surface before growth. The growth process is monitored by reflection high-energy electron diffraction (RHEED). The Bi_2Se_3 films are grown with a two-step process.[1,2] One quintuple layer (QL) Bi_2Se_3 is first grown at a low substrate temperature of 225°C. The rest of the layers are grown at a higher temperature of 265°C. The film thickness is precisely determined by the RHEED intensity oscillation (Figure S1a). *In situ* ARPES characterization of the electronic band structure also confirms the film thickness.

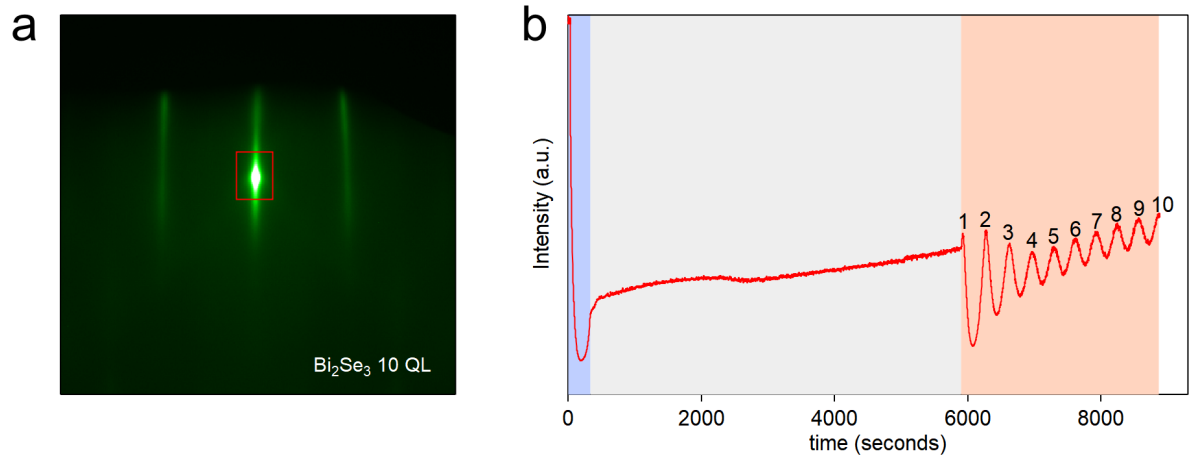

Figure S1: Layer-by-layer growth of Bi_2Se_3 films. (a) Reflection high-energy electron diffraction (RHEED) image of an as-grown 10 QL Bi_2Se_3 film on a $SrTiO_3$ substrate. (b) RHEED intensity oscillation during the Bi_2Se_3 growth. The intensity is integrated within the red box in panel (a). The blue area represents the growth of the first QL at 225 K. After the growth of the first QL, the substrate temperature is increased to 265 K (gray region). The clear RHEED intensity oscillation enables us to determine the film thickness (orange region). The growth rate is 5.5 min/QL.

SI Note 2: Atomic force microscopy (AFM) and Raman measurements of transferred Bi_2Se_3 films

Figure S2a shows a typical AFM image of a 3 QL Bi_2Se_3 film grown on a $SrTiO_3$ substrate. The surface of the film is flat with some islands formed by one additional layer, which is similar to previous studies.[3,4] After the liberation, the overall surface morphology is preserved (Figure S2b). The surface roughness of the transferred film is larger than that of the as-grown film and the edges of the islands become blurry, which can be induced by the degradation during the liberation process. We also measured the Raman spectrum of a transferred 6 QL Bi_2Se_3 film (Figure S2c). Three phonon modes are observed and their energies are consistent with the bulk values from previous measurements.[5] Our AFM and Raman measurements further confirm the high quality of the transferred films.

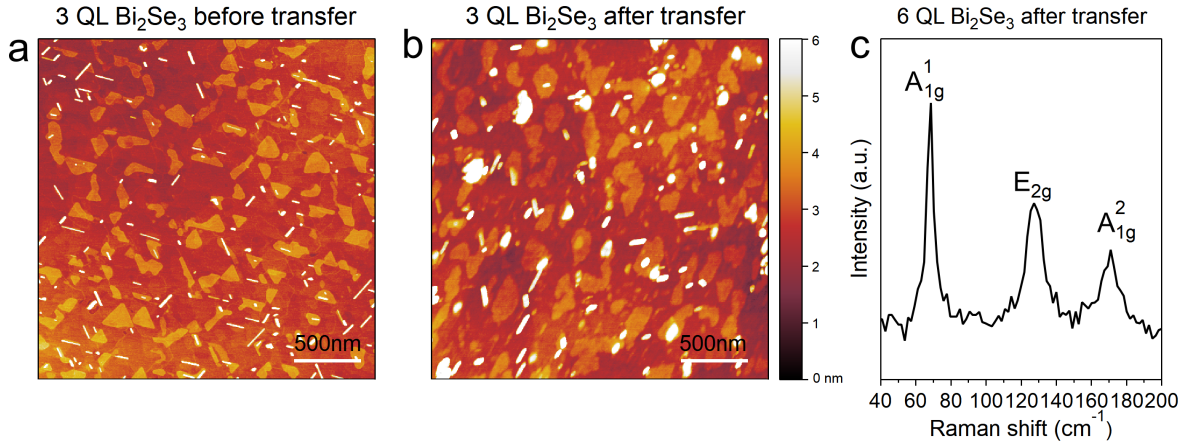

Figure S2: AFM and Raman measurements of Bi_2Se_3 films. (a) AFM image of an as-grown 3 QL Bi_2Se_3 film on a $SrTiO_3$ substrate. (b) AFM image of a transferred 3 QL Bi_2Se_3 film on Si. (c) Raman spectrum of a 6 QL Bi_2Se_3 film suspended on a 5 μm aperture measured at 300 K.

SI Note 3: Low energy cutoff in the ARPES spectrum measured by 6 eV.

It is challenging to distinctively observe the energy gap near the Dirac point for the 3 QL film before the transfer, due to the low-energy cutoff (LEC) located at −0.52 eV (Figure S3b). The LEC is induced by the work function difference between the sample and the photoemission analyzer (Figure S3a), which has been observed widely in Bi_2Se_3 using 6 eV photons.[6,7] Note that the photoelectron's kinetic energy corresponding to the LEC is always at $\phi_{\text{sample}} - \phi_{\text{detector}}$. With a much higher photon energy, the electrons near the Fermi level will be located at much higher kinetic energies: $\mathrm{E_k} = h\nu - \phi_{\text{detector}} - \mathrm{E_B}$, where $h\nu$ is the photon energy and $\mathrm{E_B}$ is the binding energy. Hence, the ARPES spectrum taken with 21.2 eV photons is not complicated by the LEC (Figure S3c).

At the thickness of 3 QL, the topological surface states (TSSs) from the top and bottom layers are expected to hybridize and form a hybridization gap.[8] This hybridization also leads to Rashba-like band splitting in the Dirac cone.[9] In our data taken with 21.2 eV photons, this hybridization is rather subtle, but the outer branch of the Rashba bands is observed in the second-derivative plot (Figure S3d). The hybridization gap is around 60 meV, which is smaller than the result (∼120 meV) in Zhang *et al.*[9] We remark that our data quality, as benchmarked by the linewidths of the TSSs (Figure S4), is higher than that in Zhang *et al.*,[9] and we have well-defined RHEED intensity oscillations (Figure S1). The difference in the hybridization gap is likely due to the different substrates ($SrTiO_3$ in our work versus graphitized SiC in Zhang *et al.*[9]), which leads to different interfacial conditions and thus different hybridization between the TSSs from the top and bottom QLs.

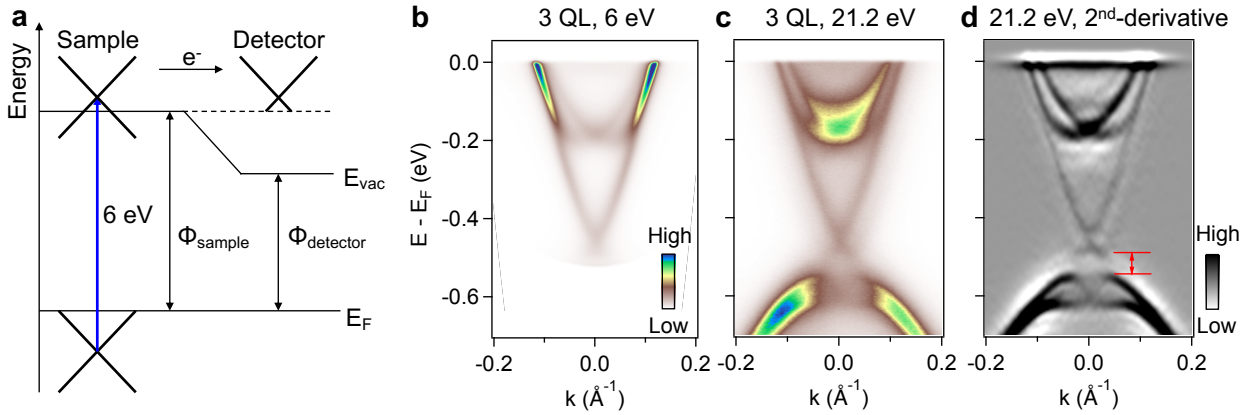

Figure S3: Illustration of the low-energy cutoff (LEC) and the hybridization gap in 3 QL Bi_2Se_3. (a) Energy diagram for the photoemission process. (b) The electronic structure of 3 QL $Bi_2Se_3/SrTiO_3$ measured by 6 eV. The LEC is at -0.52 eV. (c) 21.2 eV data on the same 3 QL sample. (d) Second-derivative plot of the 21.2 eV data in panel (c). The Rashba-like splitting in both the upper and lower branches of the Dirac cone helps us identify a bandgap near 60 meV.

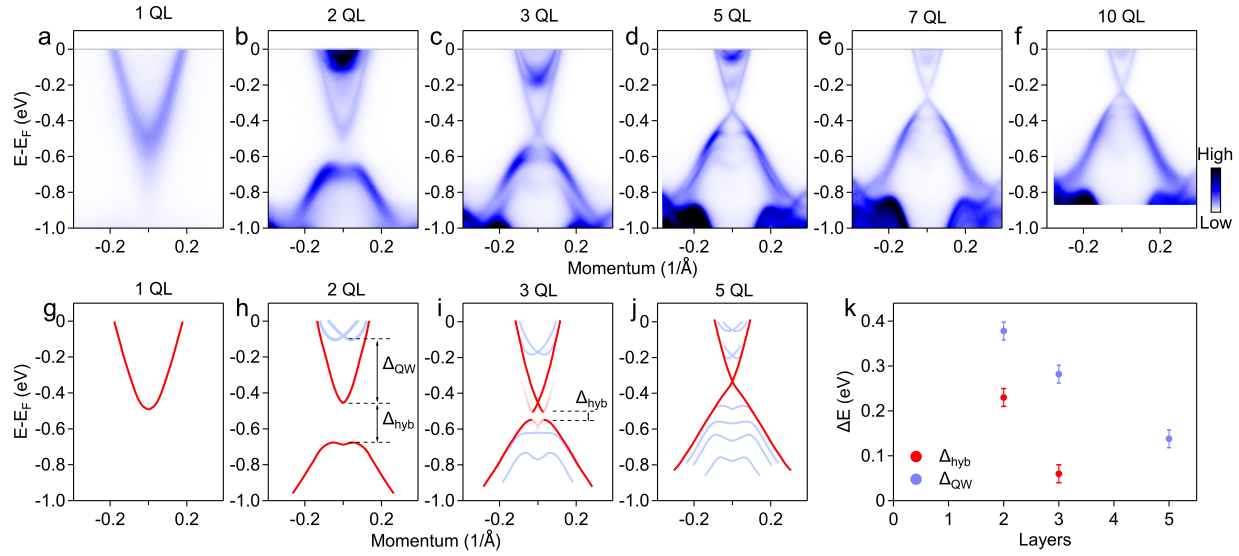

Figure S4: Thickness dependent electronic structures of Bi_2Se_3 films measured by 21.2 eV photoemission. (a-f) Electronic structures of Bi_2Se_3 films with thicknesses of 1 QL, 2 QL, 3 QL, 5 QL, 7 QL, and 10 QL, respectively. (g-j) Schematic electronic structures of Bi_2Se_3 films with thicknesses of 1 QL, 2 QL, 3 QL, and 5 QL, respectively. (k) Evolution of the hybridization gap (Δ_{hyb}) and the energy difference between the zeroth- and first-order quantum well states (Δ_{QW}), as functions of the film thickness.

SI Note 4: Origins of the Dirac gaps in as-grown Bi_2Se_3 films.

We restrict our discussion to as-grown, relatively thick Bi_2Se_3 films (thickness ≥ 5), and do not discuss the Dirac gap due to the top-bottom hybridization. The intrinsic gaps at the Dirac point are expected to be $\ll 10$ meV in these relatively thick films by theory,[8] or by previous experimental studies.[9]

There are a few possible scenarios to explain a seemingly gapped Dirac cone: 1) hybridization between the TSS and a defect resonant state;[10] 2) hybridization between the TSS and the first-order quantum well state (QWS); 3) linewidth broadening due to the finite self energy and finite resolutions (Figure S6);[11] 4) a gap in the photoemission final state.[12] First, as demonstrated by our high-quality ARPES data on as-grown films (Figure S4), there is no evidence on any films showing the defect-induced flat band near the Dirac point. Hence, Scenario #1 is unlikely. Second, the first-order QWS is located < 50 meV above the Dirac point in films thicker than 6 QL (Figure S7), and can give the impression of a gapped Dirac cone. However, the energy of the first-order QWS is thickness-dependent. As shown in Figure S5a, the Dirac gaps in 4 QL, 5 QL, and 6 QL are essentially the same ($\sim$40 meV), which renders Scenario #2 unlikely. Third, we use the photon energy dependence to distinguish Scenario #3 and #4. Based on Scenario #3, the linewidth of the Dirac band can be independent of the photon energy if it is dominated by the intrinsic electronic self energy. Notably, the Dirac gap of the 5 QL film is almost unchanged ($\sim$40 meV) when switching from 6 eV to 21.2 eV (Figure S5a,b), and is thus likely due to the self-energy-dominated linewidth broadening (Scenario #3).

On the other hand, based on Scenario #4 the Dirac gap should be a strong function of the photon energy, as the final state dispersion will drastically vary if the photon energy is changed. This seems to reflect the observations on the 10 QL film (Figure S5c,d). While we cannot completely rule out this scenario, it is surprising that such a strong final-state

effect does not affect thinner Bi_2Se_3 films (e.g., 6 eV data on the 5 QL film) or Bi_2Se_3 bulk crystals (e.g., Fig. 1 of Ref.[7]). Here we propose another possible scenario. Since 6 eV can probe $2 \sim 3$ QLs into the bulk,[13] it reveals the contributions from the buried second or third QL to the TSS in addition to that from the top QL. Note that thicker films tend to develop "pyramid-like" surface morphologies,[14] which induce additional scattering and momentum smearing for the "inner" electrons traveling across the densely spaced step edges. This can explain the Dirac gap based on Scenario #3, as observed by relatively bulk-sensitive 6 eV photoemission, but not by the surface-sensitive 21.2 eV photoemission.

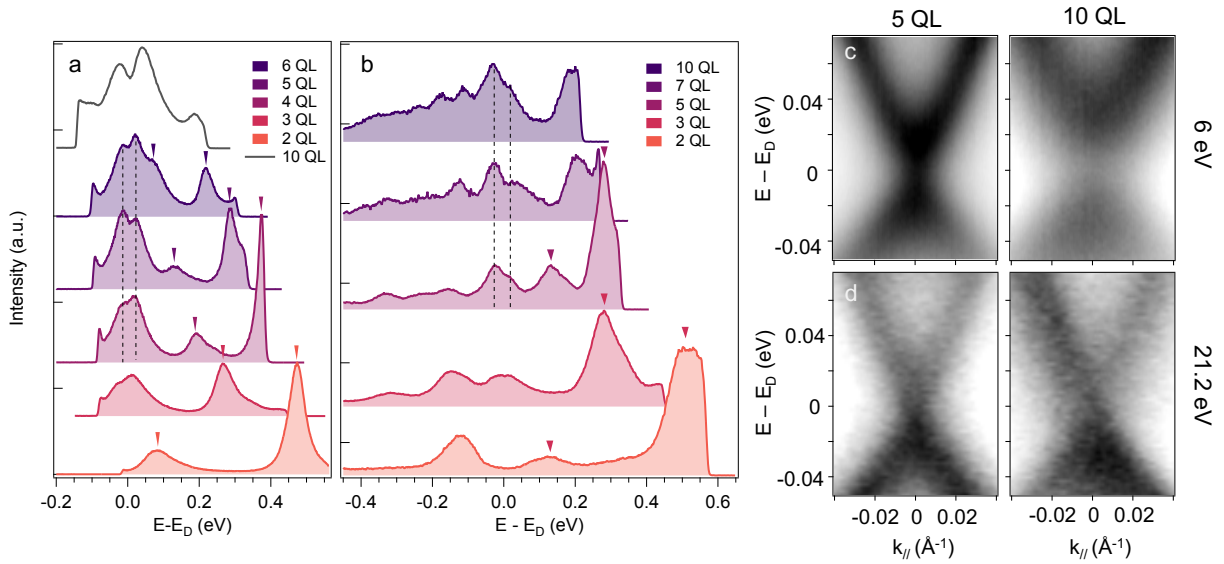

Figure S5: Distinguishing different origins for the Dirac gaps. (a,b) Energy distribution curves (EDCs) taken at zero momentum using (a) 6 eV, and (b) 21.2 eV photons. (c) Energy-momentum maps of 5 QL and 10 QL Bi_2Se_3 films using 6 eV photons. (d) Counterpart maps using 21.2 eV photons.

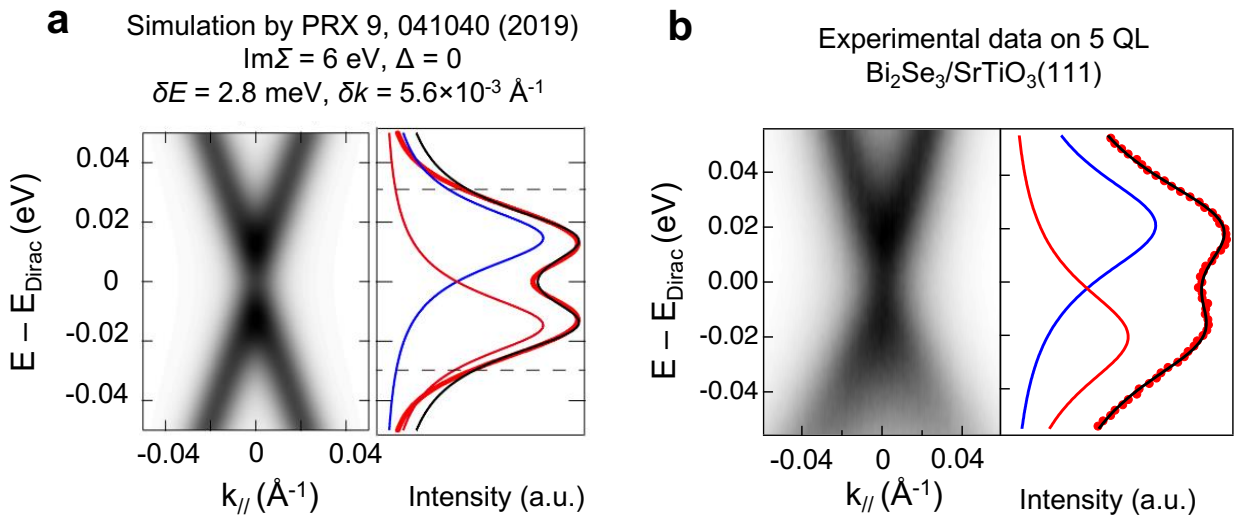

Figure S6: Gapped ARPES spectrum due to linewidth broadening. (a) Simulated spectrum with a reasonable choice of spectral parameters, taken from Phys. Rev. X 9, 041040 (2019).[11] The electronic self energy $\mathrm{Im}\Sigma = 6$ meV; the energy and momentum resolutions were chosen to be $\delta E = 2.8$ meV and $\delta k = 5.6 \times 10^{-3}$ Å^{-1}. An energy distribution curve (EDC) cutting through zero momentum was plotted and fitted to a double-Lorentzian function. (b) Our experimental ARPES spectrum from 5 QL $Bi_2Se_3/SrTiO_3(111)$, and the corresponding EDC analysis.

SI Note 5: Evolution of the quantum well states of Bi_2Se_3 films as a function of the film thickness.

The quantum well states (QWSs) in Bi_2Se_3 films are generally interpreted using the continuous model for 3D topological insulators in the ultrathin limit.[8] They originate from the quantization of the Dirac state due to c-axis confinement, and hence the Dirac state is the zeroth-order QWS. According to this model, $\Delta E_{n-0} = E(n) - E(0)$ should follow the scaling of n^2/d^2, where n is the order of the sub-band, and d is the thickness of the quantum well. We thus compare our experimental results for ΔE_{n-0} vs d on a log-log plot in Figure S7c, with the results extracted from Zhang *et al.* (Figure S7d).[9]

The evolution of our QWS energy as a function of the film thickness is qualitatively consistent with that in Zhang *et al.*[9] However, quantitatively our results are different. If we use ΔE_{1-0} as the benchmark, ΔE_{1-0} is 394 meV and 52 meV in our 2 QL and 6 QL films, but

is 450 meV and 200 meV in the counterpart films in Zhang *et al.*[9] Note that the quantitative differences can be due to the different substrates ($SrTiO_3$ in our case and graphitized SiC in Ref.[9]), and hence different quantum well configurations. To compare with the theoretical model,[8] we extract the exponent of the ΔE_{1-0} vs d relationship by doing linear fitting of the data on a log-log plot (i.e., $\ln(\Delta E_{1-0}) = a_1 + a_2 \ln(d)$). Notably, the exponent (a_2) for ΔE_{1-0} is -1.75 in our films, but this exponent was -0.78 for the films in Ref.[9] This means that our QWSs in as-grown Bi_2Se_3 films are closer to the theoretical prediction (theoretical exponent is -2) for an infinite-depth QWS. We note that the agreement between our experimental data and the theoretical model based on the infinite-depth quantum well[8] is rather surprising, considering that one side of the c-axis quantum well is vacuum and the other side is Nb-doped $SrTiO_3$. We speculate that our Bi_2Se_3 may be grown in the "step-climbing" mode,[15] where the bottom QL forms a continuous "carpet" without disruptions from the underlying substrate step edges. In such a morphology, there can be a small vacuum gap between the bottom QL and the $SrTiO_3$, which makes the c-axis quantum well more symmetric.

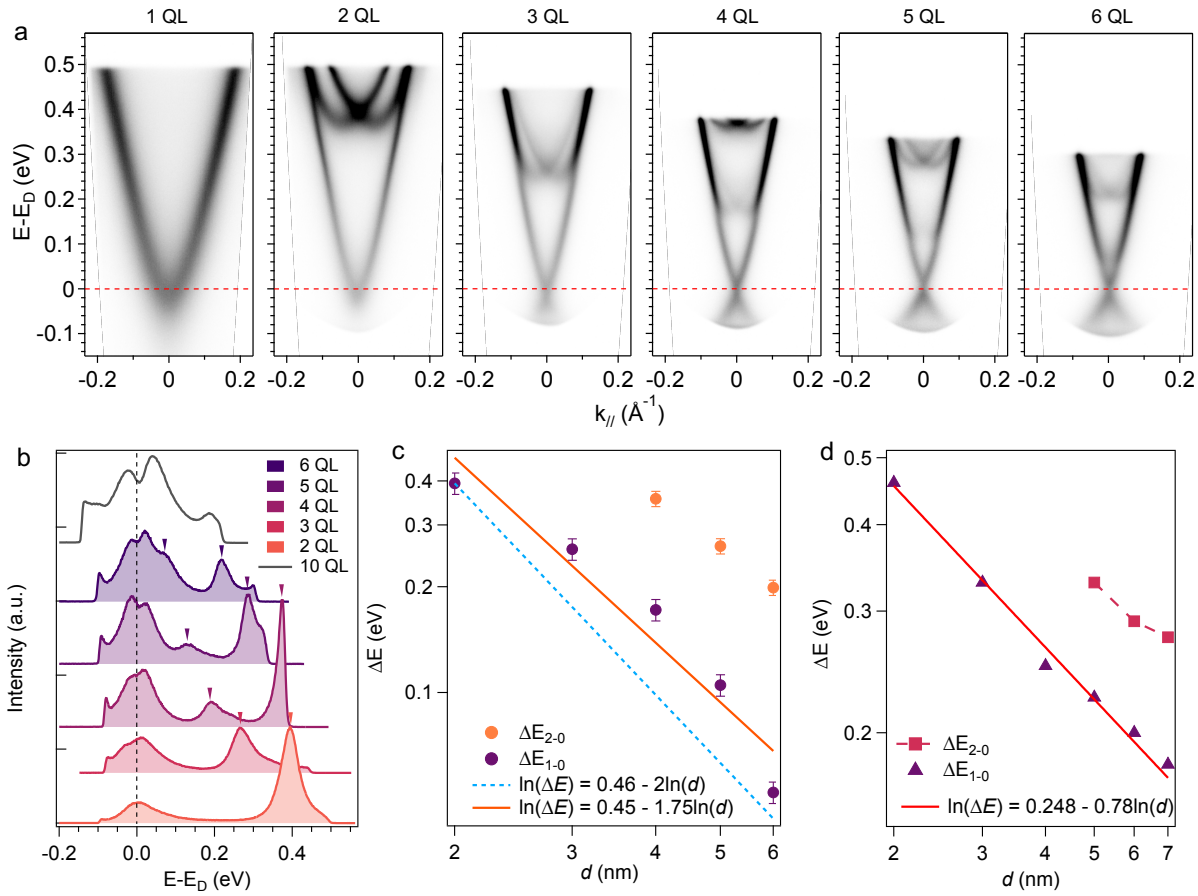

Figure S7: Evolution of the quantum well states as a function of the film thickness. (a) 6 eV ARPES data on Bi_2Se_3 thin films with thicknesses ranging from 1 to 6 QL. (b) Energy distribution curves (EDCs) taken at zero momentum. (c) Our experimental results of ΔE_{1-0} and ΔE_{2-0}, which represent the energy differences between the zeroth and first-order states and those between the zeroth and second-order states, respectively. The fitted slope on a log-log plot for ΔE_{1-0} is -1.75. (d) Extracted counterpart results from Zhang *et al.*[9]

SI Note 6: Comparison of the quantum well states in Bi_2Se_3 films before and after the transfer.

Both the QWSs and the TSSs are shifted after the transfer. The TSS shift is interpreted as a change of doping. Notably, Bi_2Se_3 can react with H_2O during the wet transfer, which produces Se vacancies and thus more electron doping ($Bi_2Se_3 + 6H_2O \rightarrow 3H_2Se\uparrow + 2Bi(OH)_3$).[16] Oxidation of chalcogenide films generally leads to hole-doping, and is thus not the dominant effect in our transfer process.[17] The energies of the QWSs are defined with respect to the zeroth order QWS, which is the Dirac state. We summarize the changes of ΔE_{n-0} for 3 QL and 5 QL films in Table S1.

Both the first-order and second-order QWS energies are substantially changed after the transfer. This is expected as the boundary conditions for the films are impacted by the chemical and thermal treatments during the transfer. The bottom layer can be compromised by H_2O and O_2; the surface layer can be additionally impacted by Se and polymer residuals (Figure S8f). Precisely modeling the boundary conditions after the transfer is very challenging and subject to future investigations. Nevertheless, we remark that surface-related chemical changes can result in a "triangular potential" near the surface.[16] One important feature of such a triangular potential is that the energy spacing between adjacent QWSs gradually decreases as the order of the QWS increases (i.e., $\Delta E_{2-1} < \Delta E_{1-0}$). This contrasts the series of QWSs in a more ideal quantum well,[8] where the energy spacing between adjacent QWSs gradually increases as the order of the QWS increases (i.e., $\Delta E_{2-1} > \Delta E_{1-0}$). For the 5 QL sample, the change of the QWS energy spacings implies that there may be a triangular potential emerging due to the surface- and/or interface-related contamination.

Table S1: The comparison of the quantum well states of the Bi_2Se_3 films before and after transfer.

Thickness	ΔE_{1-0}, before transfer (eV)	ΔE_{2-0}, before transfer (eV)	ΔE_{1-0}, after transfer (eV)	ΔE_{2-0}, after transfer (eV)
3 QL	0.26	N/A	0.28	0.46
5 QL	0.11	0.27	0.24	0.34

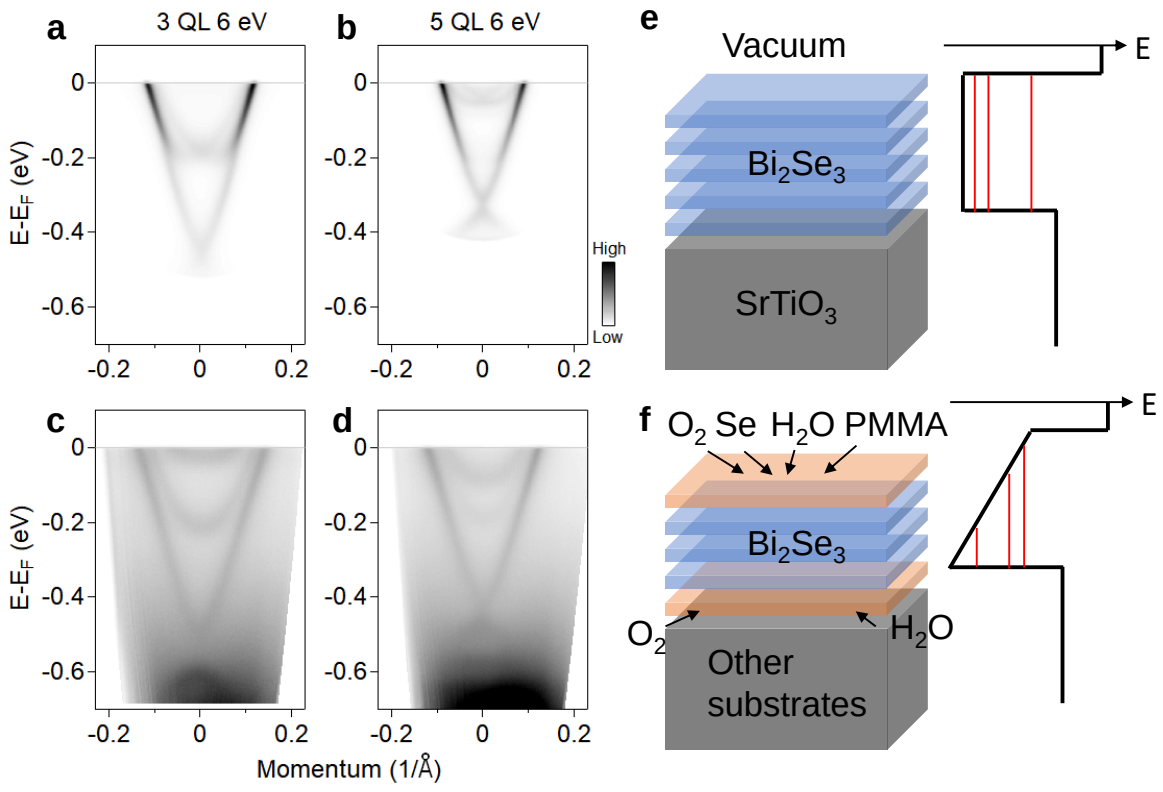

Figure S8: Changes in the QWS energies in Bi_2Se_3 films after the transfer. (a,b) 6 eV ARPES spectra of 3 QL and 5 QL films before the transfer. (c,d) Corresponding spectra after the transfer. (e,f) Illustrations of (e) the more ideal symmetric quantum well and (f) the asymmetric quantum well due to the surface- and interface-related contamination.

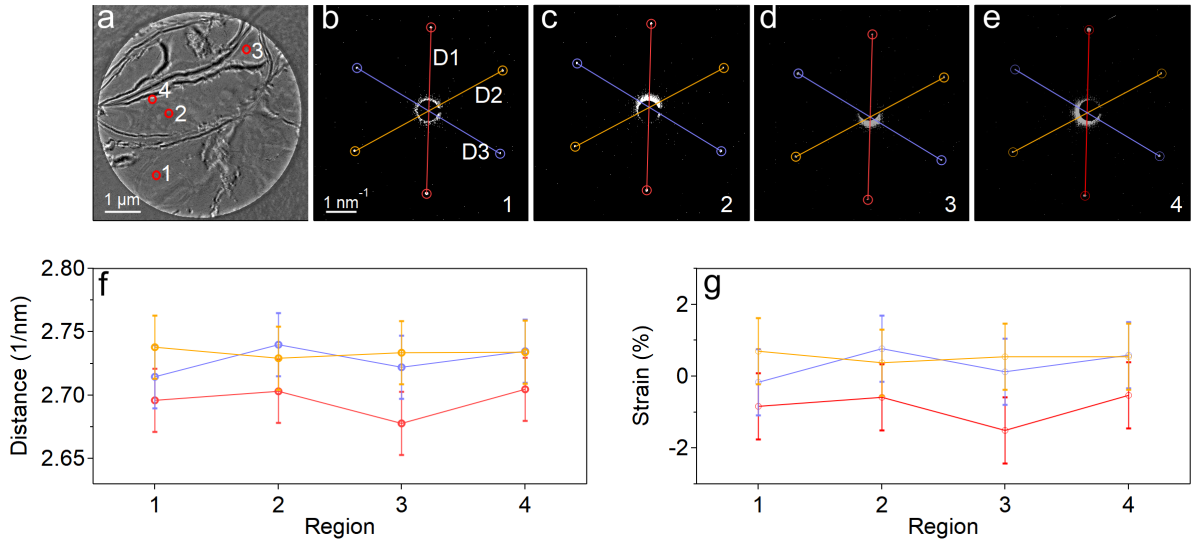

Figure S9: A 10 QL Bi_2Se_3 membrane suspended on a 5 μm SiC aperture. (a) Broad field-of-view image from transmission electron microscopy (TEM). (b-e) Selected-area electron diffraction (SAED) patterns taken at 4 selected spots, as indicated in panel (a). Each SAED pattern is integrated over an area with a diameter $\sim$ 200 nm. (f) Reciprocal lattice vectors for 3 directions. (g) Strains along the 3 directions. Due to the different locations on the membrane and different proximities to the edge of the aperture and wrinkles, if there are any measurable strains we expect the SAED patterns from the 4 locations to be measurably different. However, our results do not exhibit measurable differences between the SAED patterns from the 4 locations. Hence the strains on the free-standing membrane, if there are any, are beyond our detection limit.

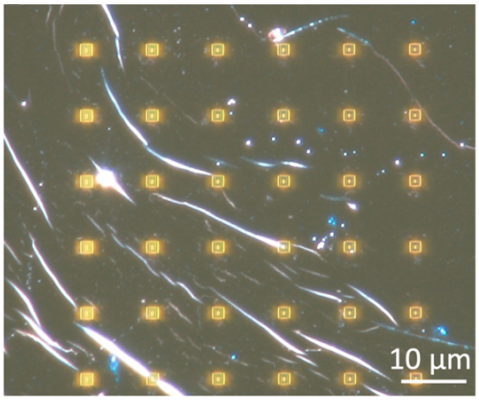

Figure S10: Optical image of a 6 QL Bi_2Se_3 film transferred on top of a 6×6 array of Si-based photonic crystal cavities. Back lighting illuminates the tears which are separated by 5-20 μm.

SI Note 7: Scanning transmission electron microscopy (STEM) characterization of suspended Bi_2Se_3 films

The liberation of millimeter-scale topological insulator films enables the construction of suspended membranes and the observation of local defects. As shown in Figure S11, we liberate a 10 QL Bi_2Se_3 film and stack the film on top of a 5 μm silicon nitride aperture. Figure S11a shows an atomically-resolved STEM top-view image and a SAED pattern of the suspended Bi_2Se_3 film taken from a typical 200 nm region of the aperture. Here our microscopy results reveal the Bismuth atomic columns due to their large atomic number ($Z = 83$). The presence of periodic atomic planes and a 6-fold symmetric diffraction pattern suggest the high quality of the film after the transfer. With a detailed scanning of the suspended film, different domains are observed in specific regions of the aperture, hosting defects at the domain boundaries (Figure S11 and S12). In Figure S11b and Figure S12a-c, a small angle (1.5°) domain boundary leads to a distinct defective atomic plane, along which every other atom is marked with vanishing intensity. We also identify point-like defects at the boundary between two domains with a larger crystallographic angular difference (7°), as shown in Figure S11c and Figure S12d-f. In Figure S11d, we extract the atomic positions around such a defect. It is clearly resolved that three atomic planes on the right-hand side (red dots in Figure S11d)

evolve into one atomic plane on the left-hand side. Two atomic columns have a coordination number of five instead of six near the topological lattice defect. We remark that even though the defective center is a point in Figure S11d, such a defect is classified as an edge dislocation, which is a line defect traversing perpendicularly into the paper.[18] Using the geometrical phase analysis (GPA) method,[19,20] we extract the strain maps for two strain components (ε_{xx} and ε_{yy}) as depicted in Figure S11e and f. The large anisotropic strain up to $\pm 20\%$ is mainly localized near the defect, yet the strain along the y direction extends to a few nm beyond. The positive and negative values on the left and right-hand side, respectively, of the ϵ_{yy} map correspond to the tensile and compressive strains (Figure S11f). These strains can affect the electronic structures in a 2 nm extended local area. The more localized ϵ_{xx} pattern reflects the change of the inter-atomic distance very close to the defect. Interestingly, the 7° angular difference between the upper and lower domains in Figure S11c leads to a quasi-periodic array of the topological defects, with a period of $\sim$ 3.7 nm (Figure S12d). A similar local strain effect in Bi_2Se_3 films grown on graphitized SiC(0001) substrates has been reported in previous STEM and scanning tunneling microscope (STM) studies.[21] We emphasize that the suspended film in our work allows for resolving the atomic-scale origin of such strains for the first time. The line defects are topological in that they will not be annihilated if the lattice is continuously deformed. Although such topological lattice defects do not lead to additional 1D topological states by themselves,[18] the substantial distortion they induce in the surrounding lattice will have nontrivial consequences in the local electronic structures.[21]

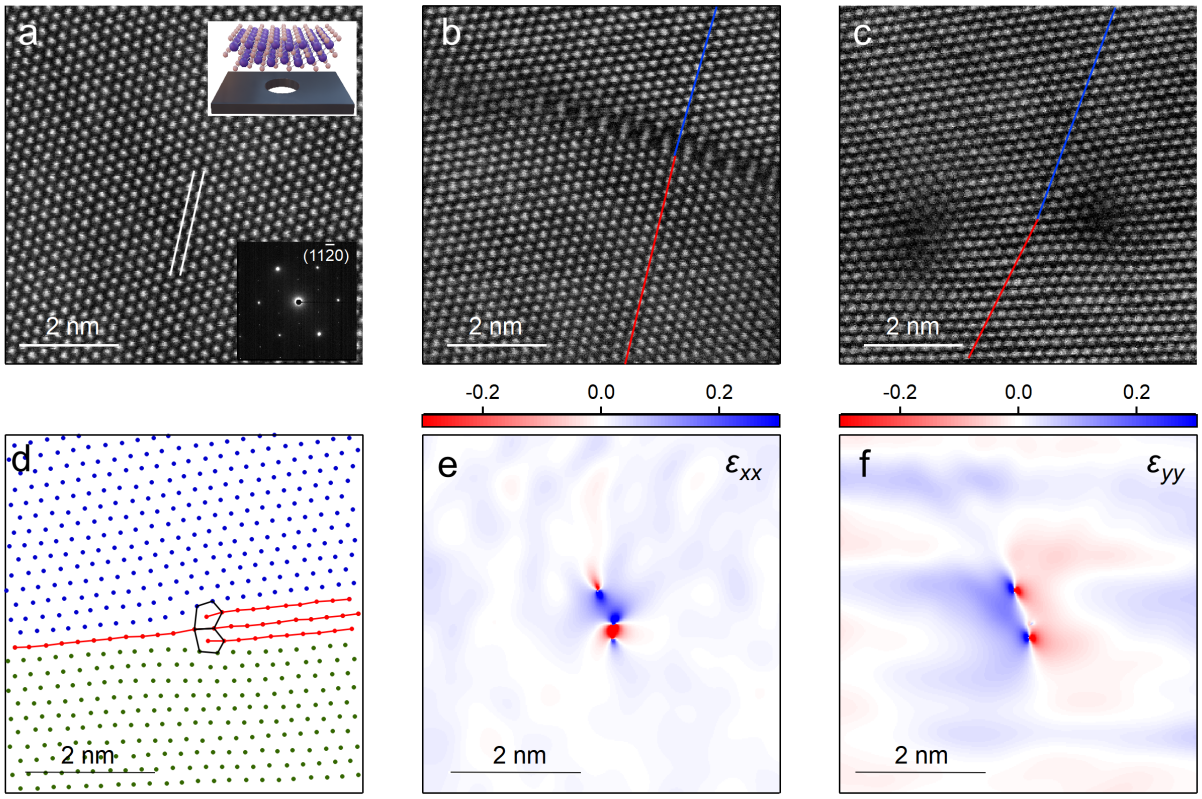

Figure S11: Atomically-resolved structural characterizations of a 10 QL Bi_2Se_3 film suspended over a 5 μm aperture. (a) STEM image taken from a defect-free region of the aperture. The spacing between the (11$\bar{2}$0) atomic planes marked by the parallel white lines is 0.22 nm. The top inset shows the schematic of the Bi_2Se_3 film suspended on an aperture. The bottom inset is the Selected Area Electron Diffraction (SAED) taken along the [0001] direction. (b) STEM image taken from a region showing a defective atomic plane. The red and blue lines mark the orientations of the two domains which have an angular difference of 1.5°. (c) STEM image taken from a region with topological defects. The red and blue lines mark the orientations of the two domains which have an angular difference of 7°. (d) The extracted atomic positions near one topological defect from (c). The blue and green dots represent the two domains and the red dots mark the atomic planes relevant for the topological defects. (e, f) The strain maps corresponding to the topological defect in (d), obtained by the geometrical phase analysis method along the horizontal (x) and vertical (y) directions, respectively.

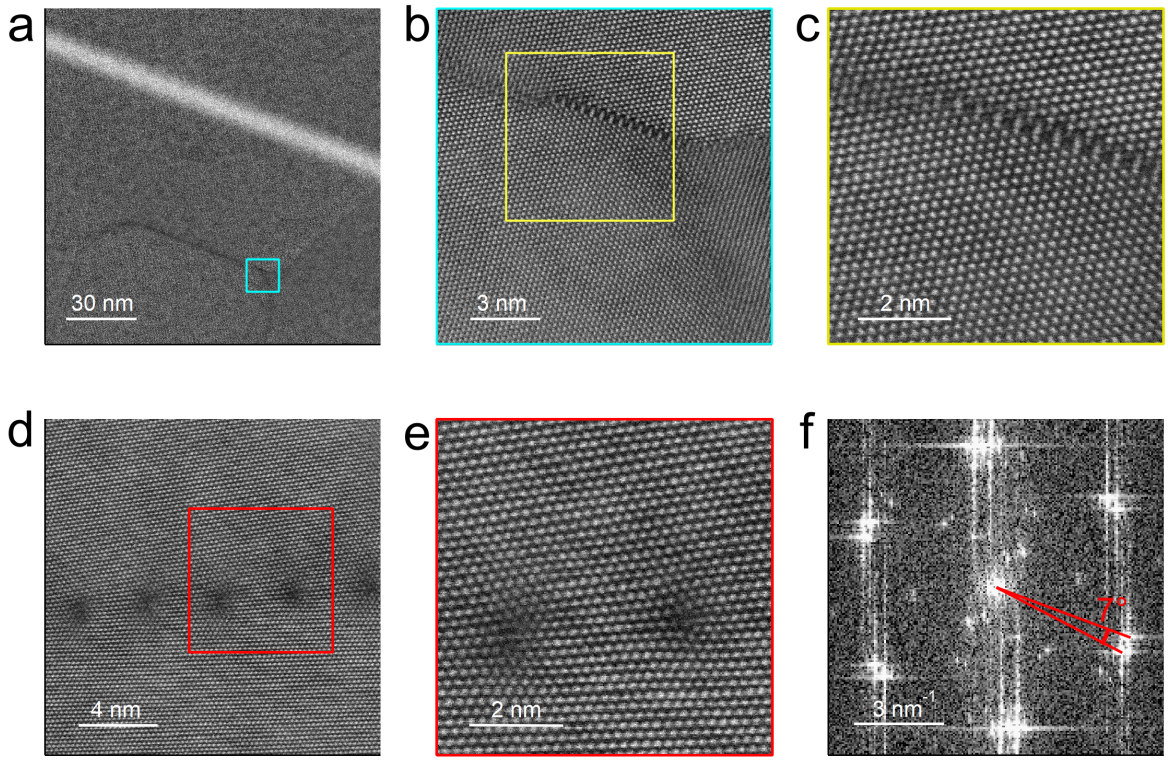

Figure S12: Additional data on the defects near the domain boundaries in suspended 10 QL Bi_2Se_3 films studied by STEM. (a) A large-scale STEM image of a 10 QL Bi_2Se_3 film suspended on a 5 μm aperture. (b, c) Zoomed-in views of the domain boundary, with the field-of-view's for (b) and (c) defined by the colored rectangles in panels (a) and (b), respectively. (d) STEM image taken from a region with a series of topological defects. (e) Zoomed-in view marked by the red box in (d). (f) The Fast Fourier Transform (FFT) of (d). An angle of 7° between the two domains is determined.

SI Note 8: Preservation of topological surface states in millimeter-scale transferred Bi_2Te_3 films

Our technique of millimeter-scale liberation can also be applied to Bi_2Te_3 films. Figure S13a and b display the Fermi surface and the band dispersion along the Γ-K direction of a 27 QL Bi_2Te_3 film grown on a $SrTiO_3$ substrate. A hexagonal Fermi surface and a quasi-linear TSS are clearly observed, in agreement with previous ARPES measurements.[22] With the same method described in the main text, we transfer the 27 QL Bi_2Te_3 film onto a Si substrate and measure the band structure by ARPES. Figure S13c and d illustrate the constant energy contour at -0.2 eV and the band dispersion along the Γ - K direction, respectively, after the transfer. The constant energy contour exhibits a six-fold symmetry which is consistent with the Fermi surface before the transfer. Similar to the transferred Bi_2Se_3 films, the Bi_2Te_3 film also exhibits a higher electron doping after the transfer. The conduction band is observed and the TSS shifts to a higher binding energy (Figure S13d). Nevertheless, the TSS is well preserved after the millimeter-scale transfer.

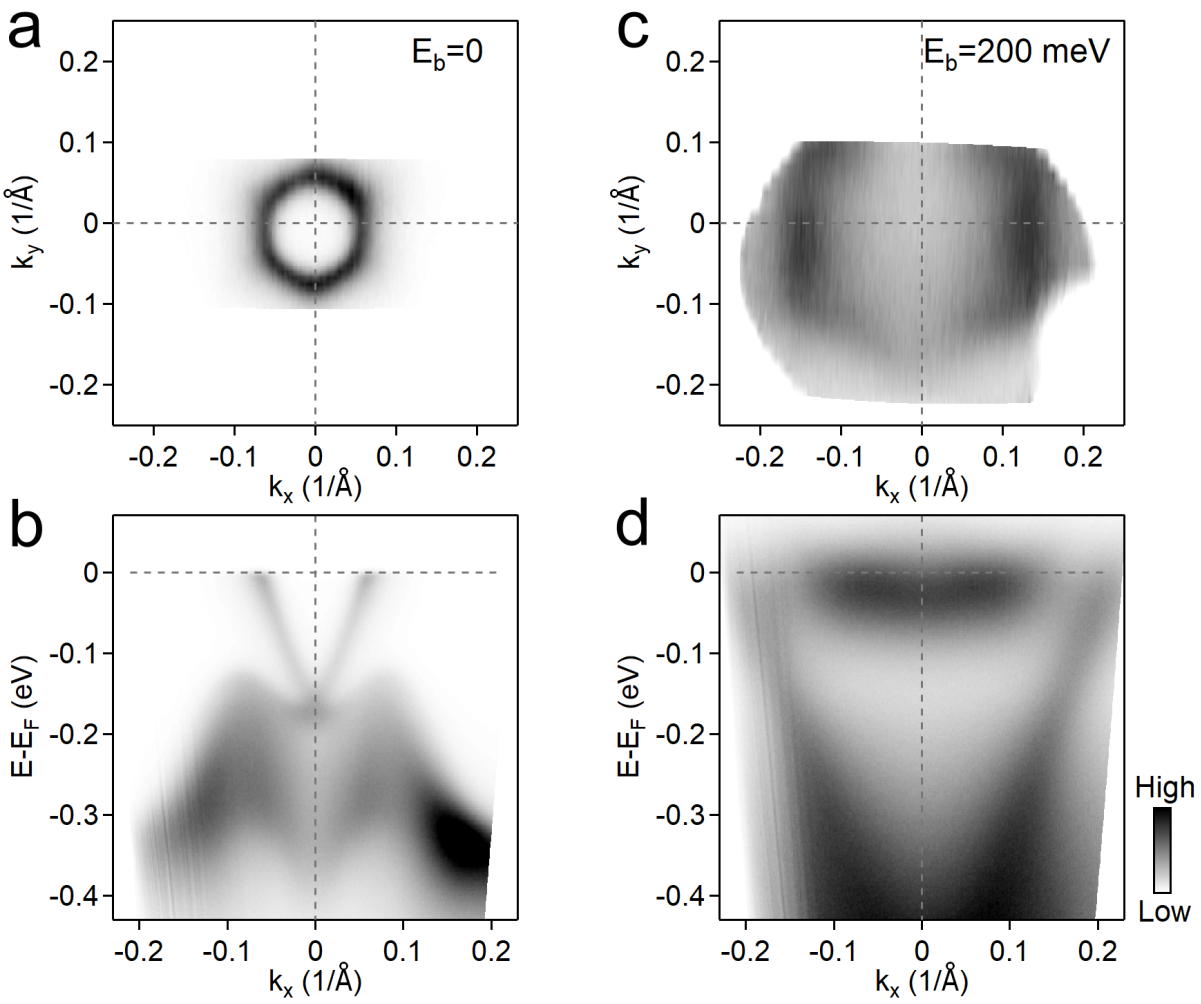

Figure S13: ARPES studies of the as-grown and transferred 27 QL Bi_2Te_3 film. (a) The Fermi surface mapping of the as-grown 27 QL Bi_2Te_3 film measured at 8.5 K. (b) The corresponding band dispersion along the Γ-K direction ($k_y = 0$). (c) The constant energy contour at a binding energy of 200 meV taken from the Bi_2Te_3 film transferred onto a Si substrate. The measurement was done at 300 K. (d) The corresponding band dispersion along the Γ-K direction for the post-transfer Bi_2Te_3 film.

References

(1) Bansal, N.; Kim, Y. S.; Edrey, E.; Brahlek, M.; Horibe, Y.; Iida, K.; Tanimura, M.; Li, G.-H.; Feng, T.; Lee, H.-D.; Gustafsson, T.; Andrei, E.; Oh, S. Epitaxial growth of topological insulator Bi_2Se_3 film on Si(111) with atomically sharp interface. *Thin Solid Films* **2011**, *520*, 224–229.

(2) Harrison, S. E.; Li, S.; Huo, Y.; Zhou, B.; Chen, Y. L.; Harris, J. S. Two-step growth of high quality Bi_2Te_3 thin films on Al_2O_3 (0001) by molecular beam epitaxy. *Applied Physics Letters* **2013**, *102*, 171906.

(3) Zhang, G.; Qin, H.; Teng, J.; Guo, J.; Guo, Q.; Dai, X.; Fang, Z.; Wu, K. Quintuple-layer epitaxy of thin films of topological insulator Bi_2Se_3. *Applied Physics Letters* **2009**, *95*, 053114.

(4) Song, C.-L. et al. Topological insulator Bi_2Se_3 thin films grown on double-layer graphene by molecular beam epitaxy. *Applied Physics Letters* **2010**, *97*, 143118.

(5) Zhang, J.; Peng, Z.; Soni, A.; Zhao, Y.; Xiong, Y.; Peng, B.; Wang, J.; Dresselhaus, M. S.; Xiong, Q. Raman Spectroscopy of Few-Quintuple Layer Topological Insulator Bi_2Se_3 Nanoplatelets. *Nano Letters* **2011**, *11*, 2407–2414.

(6) Sobota, J. A.; Yang, S.-L.; Kemper, A. F.; Lee, J. J.; Schmitt, F. T.; Li, W.; Moore, R. G.; Analytis, J. G.; Fisher, I. R.; Kirchmann, P. S.; Devereaux, T. P.; Shen, Z.-X. Direct Optical Coupling to an Unoccupied Dirac Surface State in the Topological Insulator Bi2Se3. *Physical Review Letters* **2013**, *111*, 136802.

(7) Sobota, J.; Yang, S.-L.; Leuenberger, D.; Kemper, A.; Analytis, J.; Fisher, I.; Kirchmann, P.; Devereaux, T.; Shen, Z.-X. Ultrafast electron dynamics in the topological insulator Bi2Se3 studied by time-resolved photoemission spectroscopy. *Journal of Electron Spectroscopy and Related Phenomena* **2014**, *195*, 249–257.

(8) Liu, C.-X.; Zhang, H.; Yan, B.; Qi, X.-L.; Frauenheim, T.; Dai, X.; Fang, Z.; Zhang, S.-C. Oscillatory crossover from two-dimensional to three-dimensional topological insulators. *Physical Review B* **2010**, *81*, 041307.

(9) Zhang, Y. et al. Crossover of the three-dimensional topological insulator Bi_2Se_3 to the two-dimensional limit. *Nature Physics* **2010**, *6*, 584–588.

(10) Xu, Y.; Chiu, J.; Miao, L.; He, H.; Alpichshev, Z.; Kapitulnik, A.; Biswas, R. R.; Wray, L. A. Disorder enabled band structure engineering of a topological insulator surface. *Nature Communications* **2017**, *8*, 14081.

(11) Chen, Y. et al. Topological Electronic Structure and Its Temperature Evolution in Antiferromagnetic Topological Insulator $MnBi_2Te_4$. *Physical Review X* **2019**, *9*, 041040.

(12) Miller, T. L.; Ärrälä, M.; Smallwood, C. L.; Zhang, W.; Hafiz, H.; Barbiellini, B.; Kurashima, K.; Adachi, T.; Koike, Y.; Eisaki, H.; Lindroos, M.; Bansil, A.; Lee, D.-H.; Lanzara, A. Resolving unoccupied electronic states with laser ARPES in bismuth-based cuprate superconductors. *Physical Review B* **2015**, *91*, 085109.

(13) Seah, M. P.; Dench, W. A. Quantitative electron spectroscopy of surfaces: A standard data base for electron inelastic mean free paths in solids. *Surface and Interface Analysis* **1979**, *1*, 2–11.

(14) Ginley, T.; Wang, Y.; Law, S. Topological Insulator Film Growth by Molecular Beam Epitaxy: A Review. *Crystals* **2016**, *6*, 154.

(15) Ding, D.; Wang, S.; Xia, Y.; Li, P.; He, D.; Zhang, J.; Zhao, S.; Yu, G.; Zheng, Y.; Cheng, Y.; Xie, M.; Ding, F.; Jin, C. Atomistic Insight into the Epitaxial Growth Mechanism of Single-Crystal Two-Dimensional Transition-Metal Dichalcogenides on Au(111) Substrate. *ACS Nano* **2022**, *16*, 17356–17364.

(16) Benia, H. M.; Lin, C.; Kern, K.; Ast, C. R. Reactive Chemical Doping of the Bi_2Se_3 Topological Insulator. *Physical Review Letters* **2011**, *107*, 177602.

(17) Bai, Y. et al. Quantized anomalous Hall resistivity achieved in molecular beam epitaxy-grown MnBi2Te4 thin films. *National Science Review* **2024**, *11*, nwad189.

(18) Ran, Y.; Zhang, Y.; Vishwanath, A. One-dimensional topologically protected modes in topological insulators with lattice dislocations. *Nature Physics* **2009**, *5*, 298–303.

(19) Hÿtch, M. J.; Snoeck, E.; Kilaas, R. Quantitative measurement of displacement and strain fields from HREM micrographs. *Ultramicroscopy* **1998**, *74*, 131–146.

(20) Johnson, C. L.; Hÿtch, M. J.; Buseck, P. R. Nanoscale waviness of low-angle grain boundaries. *Proceedings of the National Academy of Sciences* **2004**, *101*, 17936–17939.

(21) Liu, Y.; Li, Y. Y.; Rajput, S.; Gilks, D.; Lari, L.; Galindo, P. L.; Weinert, M.; Lazarov, V. K.; Li, L. Tuning Dirac states by strain in the topological insulator Bi_2Se_3. *Nature Physics* **2014**, *10*, 294–299.

(22) Chen, Y. L.; Analytis, J. G.; Chu, J. H.; Liu, Z. K.; Mo, S. K.; Qi, X. L.; Zhang, H. J.; Lu, D. H.; Dai, X.; Fang, Z.; Zhang, S. C.; Fisher, I. R.; Hussain, Z.; Shen, Z. X. Experimental Realization of a Three-Dimensional Topological Insulator, Bi_2Te_3. *Science* **2009**, *325*, 178–181.